A&A 528, A136 (2011)
DOI: 10.1051/0004-6361/201015866


Astronomy & Astrophysics

# *XMM-Newton* observations of the superbubble in N 158 in the LMC

M. Sasaki[1], D. Breitschwerdt[2], V. Baumgartner[3], and F. Haberl[4]

[1] Institut für Astronomie und Astrophysik, Universität Tübingen, Sand 1, 72076 Tübingen, Germany
e-mail: sasaki@astro.uni-tuebingen.de
[2] Department of Astronomy and Astrophysics, Berlin Institute of Technology, Hardenbergstr. 36, 10623 Berlin, Germany
[3] Institut für Astronomie, Universität Wien, Türkenschanzstr. 17, 1180 Vienna, Austria
[4] Max-Planck-Institut für extraterrestrische Physik, Giessenbachstraße, 85748 Garching, Germany

Received 5 October 2010 / Accepted 1 February 2011

**ABSTRACT**

*Aims.* We study the diffuse X-ray emission observed in the field of view of the pulsar B 0540–69 in the Large Magellanic Cloud (LMC) by *XMM-Newton*. We wish to understand the nature of this soft diffuse emission, which coincides with the superbubble in the H II region N 158, and improve our understanding of the evolution of superbubbles.
*Methods.* We analyse the *XMM-Newton* spectra of the diffuse emission. Using the parameters obtained from the spectral fit, we perform calculations of the evolution of the superbubble. The mass loss and energy input rates are based on the initial mass function (IMF) of the observed OB association inside the superbubble.
*Results.* The analysis of the spectra shows that the soft X-ray emission arises from hot shocked gas surrounded by a thin shell of cooler, ionised gas. We show that the stellar winds alone cannot account for the energy inside the superbubble, but the energy release of 2−3 supernova explosions in the past ∼1 Myr provides a possible explanation.
*Conclusions.* The combination of high sensitivity X-ray data, which permits a spectral analysis, and analytical models for superbubbles can provide insight into the evolutionary state of interstellar bubbles, if the stellar content is known.

**Key words.** shock waves – ISM: bubbles – evolution – HII regions – X-rays: ISM

## 1. Introduction

Early observations in the radio and the optical have shown that the interstellar medium (ISM) in the Milky Way mainly consists of cool clouds ($T \lesssim 10^2$ K) of neutral hydrogen embedded in the warm ($T \simeq 10^4$ K) intercloud medium of partially ionised hydrogen. Since the 1970s, observations in the ultraviolet (UV) and X-rays have detected hot gas at coronal temperatures ($T \simeq 10^{5-6}$ K) in the ISM. The heat source of the ISM are massive OB stars, which inject energy through their radiation, stellar winds, and finally by supernova explosions. As these processes are often correlated in space and time, superbubbles with sizes of typically 100−1000 pc are created in the ISM. Therefore, supernova remnants (SNRs) and superbubbles are among the prime sources controlling the morphology and the evolution of the ISM, and their observation is of key interest to understanding the galactic matter cycle. However, they radiate copiously in the soft X-rays below 2 keV, an energy range that is difficult to study in the Milky Way because of absorption by the Galactic disk.

The LMC, which is a dwarf irregular but appear to contain spiral structure, is one of the closest neighbours of our Galaxy. Its proximity with a distance of 48 kpc (Macri et al. 2006) and modest extinction along the line of sight (average Galactic foreground $N_{\rm H} = 1.6 \times 10^{21}$ cm$^{-2}$) make it the ideal laboratory for exploring the global structure of the ISM in a galaxy. The well-known and well-studied extended emission region in the LMC is the 30 Doradus region and the region south of it, which harbour star-formation sites, superbubbles, and SNRs. *ROSAT* data of the superbubbles in the LMC have been studied in detail by, e.g., Chu et al. (1995) and Dunne et al. (2001).

N 158 (Henize 1956) is an H II region in these active regions of the LMC. It is elongated in the north-south direction and consists of a superbubble in the north and a more compact bright region in the south. It is known to host two OB associations LH 101 and LH 104 (Lucke & Hodge 1970). While LH 101 in the southern part of N 158 seems to power the very bright region in H$\alpha$, LH 104 is found in the superbubble in the northern part of N 158 and is dominated by B stars (Schild & Testor 1992), mainly consisting of a young population with an age of 2−6 Myr (Testor & Niemela 1998). Dunne et al. (2001) analysed the *ROSAT* data and suggested that the X-ray emission seen at the position of N 158 is associated with the H II region. N 158 is located near the X-ray bright pulsar (PSR) in the LMC B 0540−69, which had been observed for calibration purposes by the X-ray Multi-Mirror Mission *XMM-Newton* (Jansen et al. 2001; Aschenbach et al. 2000). The field of view of the European Photon Imaging Cameras (EPICs, Strüder et al. 2001; Turner et al. 2001) of these observations when performed in full frame mode, covers the northern part of N 158 and allows us to study the X-ray emission from the superbubble.

## 2. Data

The pulsar B 0540−69 in the LMC is a Crab-like pulsar with a pulsar wind nebula (PWN), which has been spatially resolved and studied with the *Chandra* X-ray Observatory (Petre et al. 2007). To study the diffuse emission in the vicinity of B 0540−69, we chose observations for which the EPICs were operated in full frame mode. The observation IDs are 0117510201, 0117730501, and 0125120101. The observations were all carried out using the medium filter. Starting from the observational

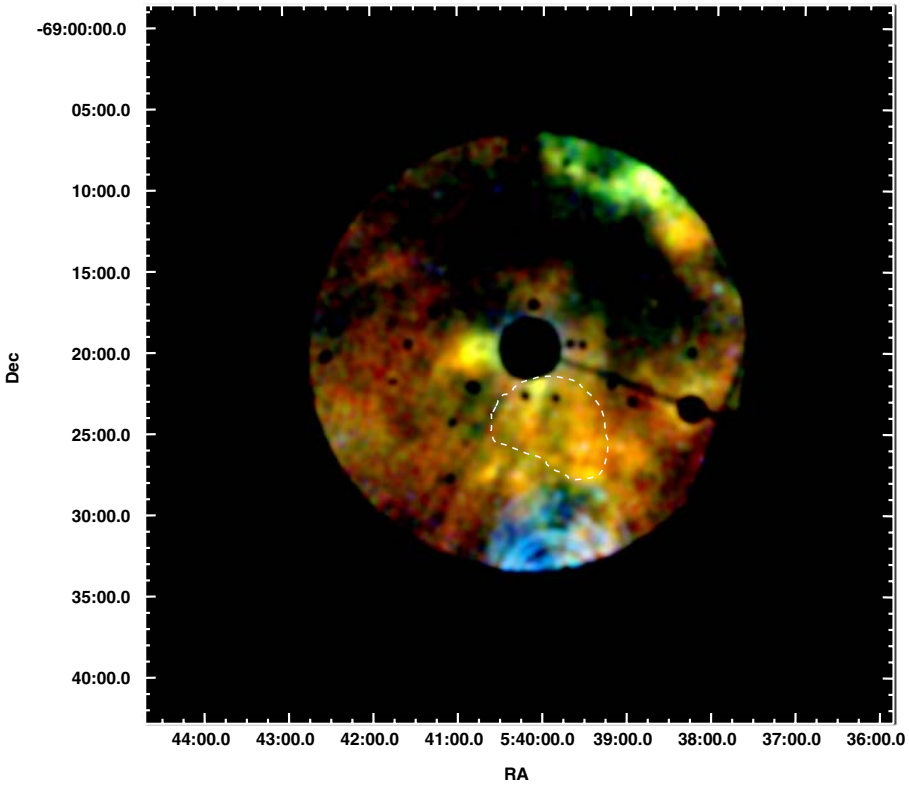


**Fig. 1.** *XMM-Newton* EPIC mosaic image of the PSR B 0540−69 and its surroundings in true colour presentation (red: 0.3−0.8 keV, green: 0.8−1.5 keV, blue: 1.5−2.3 keV). The bright X-ray emission from PSR B 0540−69 at ∼RA = $05^{h}40^{m}$, Dec = –69°20′, other point sources, and the out-of-time events have been removed from the data. The arc-shaped features in the south are caused by stray light from the bright X-ray source LMC X-1. The position of the superbubble in the H II region N 158 is shown with a dashed line.

**Table 1.** *XMM-Newton* data used for the analysis.

| Obs. ID | EPIC | Start Date | Effective Exposure [ks] |
|---|---|---|---|
| 01175102 | PN | 2000-02-11 | 8.3 |
| 01175102 | MOS1,2 | | 3.5 |
| 01177305 | PN | 2000-02-17 | 8.3 |
| 01177305 | MOS1,2 | | 9.8 |
| 01251201 | PN | 2000-05-26 | 29. |
| 01251201 | MOS1,2 | | 27. |

**Notes.** All the analysed data were obtained in full frame mode using the medium filter.

data files (ODFs), the data are processed with the *XMM-Newton* Science Analysis System (XMMSAS) version 10.0.0. For EPIC PN, only single and double pattern events are used, whereas for the MOS1 and 2, singles to quadruples are selected. The exposure times that we obtain after filtering out the time intervals with background flares are listed in Table 1.

### 2.1. EPIC image

After filtering out the background flares, we created a mosaic image out of the full frame mode data of EPIC PN, MOS1, and MOS2 for all three observations (Fig. 1). To enhance the not-so-bright diffuse emission, we filtered out all point sources found using a source detection routine as well as the so-called out-of-time events of EPIC PN. The images were smoothed using a Gaussian filter. The mosaic image shown in Fig. 1 is a true colour image using red colour for the 0.3−0.8 keV band, green for 0.8−1.5 keV, and blue for 1.5−2.3 keV. The extended emission of the interstellar gas is clearly soft with no emission above ∼3 keV. The comparison with the H$\alpha$ image of the Magellanic Cloud emission line survey (MCELS) in Fig. 2 shows that the relatively bright extended region in the south of the PSR coincides well with a superbubble in the H II region N 158 (Henize 1956), which contains the OB association LH 104 (Lucke & Hodge 1970). To study the spectral properties of the diffuse emission, we selected two regions: region 1, which covers the brighter spot in the east of the PSR, and a region that covers the superbubble in the H II region N 158. The regions are shown in the left panel in Fig. 2. The PSR and the PWN around it have an extent of about 1′. They were completely removed from the data. The soft, extended emission east to the PSR is not directly connected to the PWN and has, as we see in Sect. 2.2.4, a perfectly thermal spectrum. We therefore assume that it is not related to the PWN.

### 2.2. EPIC spectra

For the spectral analysis of an extended diffuse emission the contribution of the background is significant. Since the emission fills a large part of the detector, we are unable to extract a local background close to the source emission. We note that as the effective area of the mirrors depends on the off-axis angle, photons are subject to vignetting while particles are not. The high-energy particles that interact with the material surrounding the detector, however, produce fluorescence, which varies with position on the detector, especially for the PN detector. In addition, the spectral response depends on the position on the detector. A detailed description of the *XMM-Newton* background is given by Read & Ponman (2003) and Carter & Read (2007), and a comparison of the different methods to estimate the background can be found in, e.g., Sasaki et al. (2004).

#### 2.2.1. Blank-sky background

The *XMM-Newton* EPIC background working group has created the so-called blank-sky data for each EPIC and CCD read-out

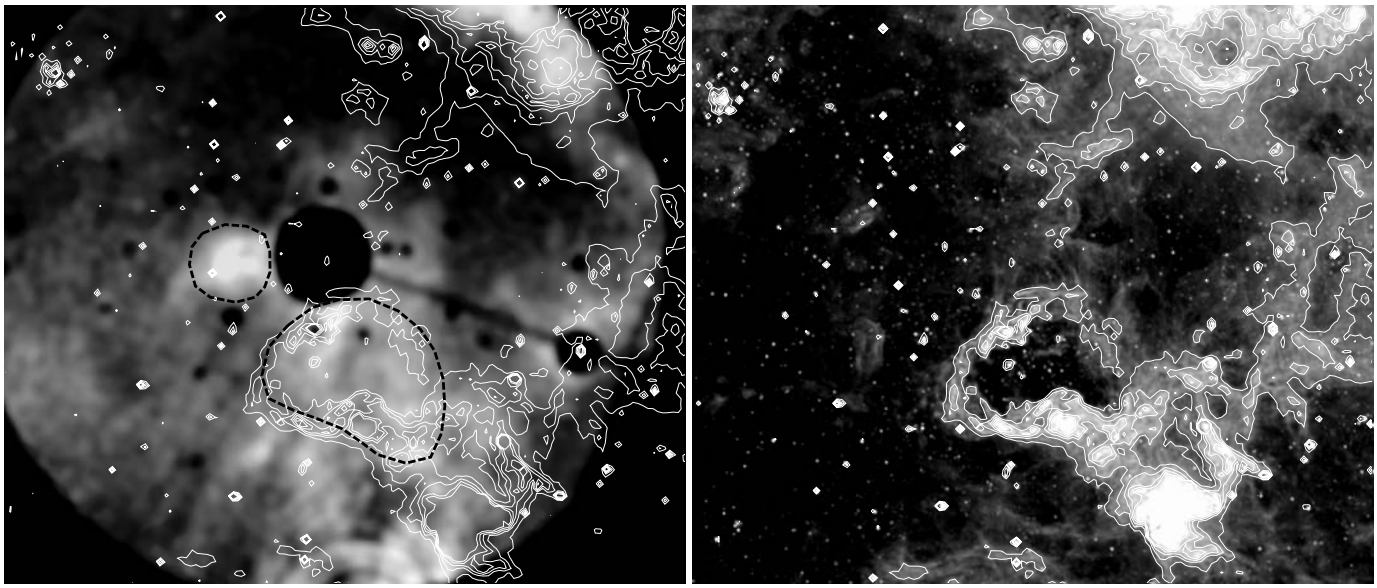

**Fig. 2.** A zoom-in on the *XMM-Newton* EPIC mosaic image (*left*) with regions used for the spectral analysis (black dashed line) and H$\alpha$ contours (MCELS) and the H$\alpha$ image with the same contours (*right*).

mode (Carter & Read 2007). The blank-sky data were merged from data of different pointings after the point sources were eliminated from the data. These data sets comprise the detector background and an average cosmic X-ray background.

Before extracting the spectra, we first corrected both the observed data and the blank-sky data for vignetting using the XMMSAS command `evigweight`. The auxiliary response file (ARF) and the response matrix file (RMF) were then created by assuming that the source is on-axis. The background spectrum was extracted from the blank-sky data at the same location on the detector as the source spectrum.

#### 2.2.2. Background from the same data

For comparison, we also extracted a background spectrum from the same data as the source spectrum, using a region in the dark part north of B 0540−69. However, after subtracting the background, the spectrum of the soft diffuse emission still has a hard tail and is overcorrected exactly at the energies of the fluorescence lines. Therefore, as expected, extracting the background for the source spectrum from the same data at a different position on the detector seems to be inappropriate.

#### 2.2.3. Closed filter wheel data

Another way to deal with the background is to use a local background from the same observation, but take care of the detector background by using the closed filter wheel data, as also supplied by the *XMM-Newton* EPIC background working group. To estimate the X-ray background, i.e., additional emission that is typical of the observed area and might also contribute to the spectrum of the superbubble, we extract a region next to the superbubble in the east, which shows faint diffuse emission. After subtracting the closed filter wheel spectrum extracted for each region at the corresponding position of the detector with the same shape, the spectrum of the faint diffuse emission in the east is fitted with a thermal model. This fitted spectrum is then included in the model of the spectra of the superbubble and region 1.

To verify whether the emission in the east is suitable for use as the local X-ray background, we estimated the flux for (i) the superbubble, (ii) the region east to it used as the local background, and (iii) the blank-sky background. We assumed a plane-parallel shock model for the superbubble and a non-equilibrium ionisation (NEI) model for the eastern region, and that both have LMC abundances (see Sect. 2.2.4 for details). A combination of a thermal and a non-thermal spectrum is assumed for the blank-sky background. From these spectra, we get the following fluxes, where the 90% confidence errors are given in brackets: $F_{0.2\text{–}3.0\ \mathrm{keV}}$(superbubble) = 1.4 (1.2–1.5) $\times\ 10^{-12}$ erg s$^{-1}$ cm$^{-2}$, $F_{0.2\text{–}3.0\ \mathrm{keV}}$(east) = 4.8 (4.0–5.3) $\times\ 10^{-13}$ erg s$^{-1}$ cm$^{-2}$, and $F_{0.2\text{–}3.0\ \mathrm{keV}}$(blank-sky) = 1.5 (1.4–1.6) $\times\ 10^{-13}$ erg s$^{-1}$ cm$^{-2}$. The flux of the X-ray background in the blank-sky data is about 10% that of the superbubble. The emission from the ISM in the east is about three times higher than the blank sky. If we were to use the blank-sky data to estimate the X-ray background, we might underestimate the background. However, if we use the local emission, we will overestimate the background as we may also expect to find hot gas in the ISM next to the superbubble because of possible breakouts. The difference between the flux of the eastern region and the blank sky is about 20% of the superbubble flux, which needs to be taken into consideration as an additional uncertainty in the flux of the superbubble.

Otherwise, the results for the spectral fits obtained with the closed filter wheel data and those obtained with the blank-sky data are consistent with each other within the confidence range of the spectral fit parameters. Therefore, in the following, we discuss the fit results obtained with the blank-sky data.

#### 2.2.4. Spectral fits

The spectra were fitted with thermal plasma models in XSPEC. We fitted the spectra of the different EPICs simultaneously with model parameters that are linked to each other. In both spectra, emission peaks are found in the energy interval between 0.5 keV and 1.5 keV that can be interpreted as emission lines of highly ionised elements. The X-ray emission is absorbed by the Galaxy in the foreground ($N_{\mathrm{H\,fg}}$) and by the matter in the LMC along the line of sight ($N_{\mathrm{H\,MC}}$) with abundances half of solar values

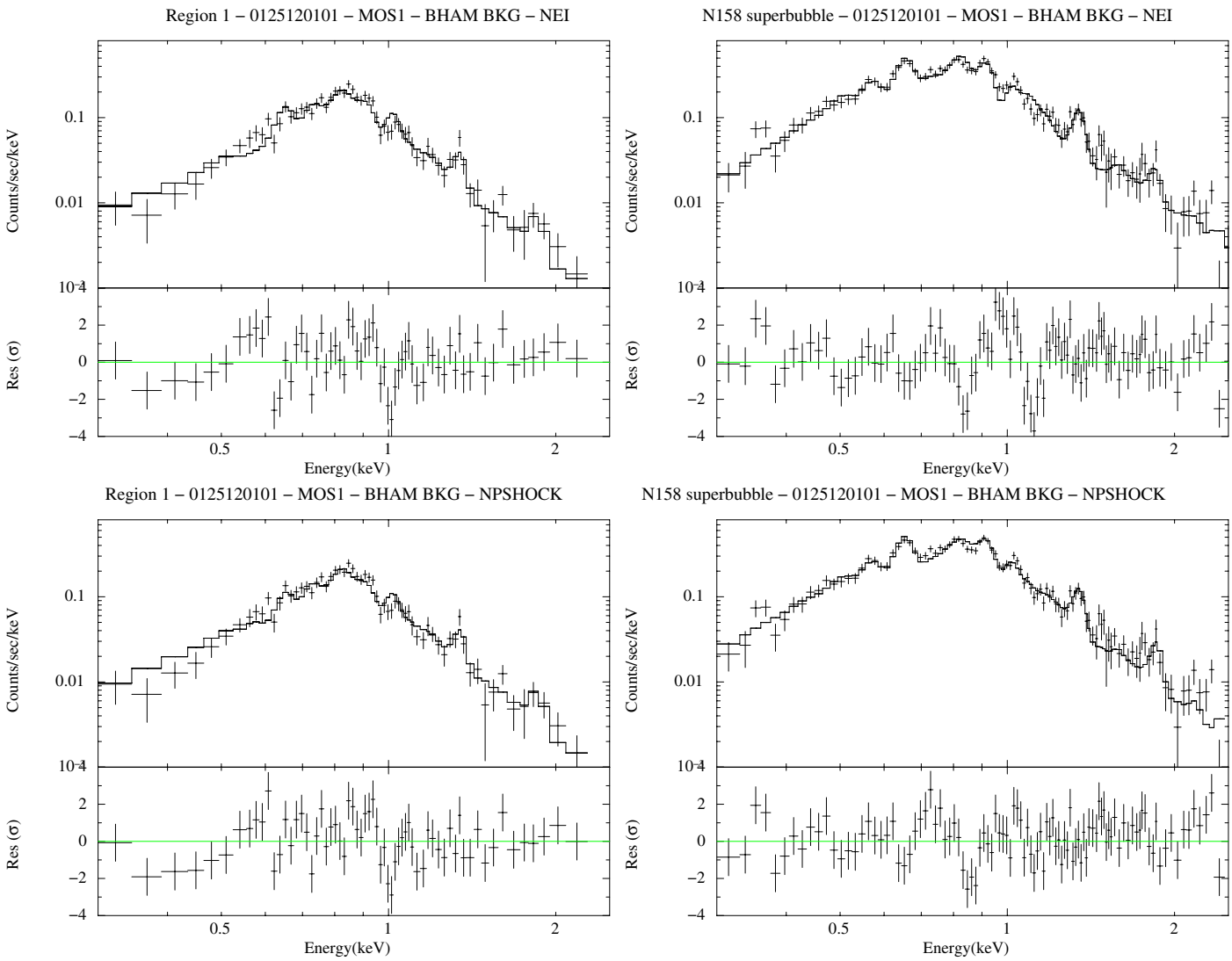


**Fig. 3.** Spectra of the diffuse emission in the field of view of PSR B 0540−69 extracted from the *XMM-Newton* EPIC MOS1 data of the Obs. ID 01251201. The *left panels* show the spectra of region 1 located east of the PSR, the *right panels* show the spectra of the superbubble in the H II region N 158. The upper diagrams show the fit with the NEI model, the lower diagrams with the NPSHOCK model.

(Russell & Dopita 1992). The Galactic foreground column density is $N_{\mathrm{H\,fg}} = 7.0 \times 10^{20}$ cm$^{-2}$ in this region (Dickey & Lockman 1990). The spectra are more accurately reproduced by a NEI model (Borkowski 2000) than by the spectral models assuming collisional ionisation equilibrium (CIE). Figure 3 shows the MOS1 spectra of the Obs. ID 01251201 with the best-fit models. In the following, 90% errors are given for the parameters.

Since the first fits with CIE yielded no satisfactory results, we used the NEI model in XSPEC with the effective temperature $kT$, the ionisation timescale $\tau = n_{\mathrm{e}}t$, and the abundance as fit parameters. The ionisation timescale $\tau$ is an indicator of the state of the plasma after the gas has been ionised. For small ionisation timescales $\tau = n_{\mathrm{e}}t < 10^{12}$ s cm$^{-3}$, the electrons and ions are still not in thermal equilibrium. For this model component, we also assumed the sub-solar LMC abundance $\zeta_{\mathrm{LMC}} = 0.5$. The fit of the spectra of the superbubble emission is still not very good with a reduced $\chi^2$ of 1.75. The emission is most likely caused by the shock from the stellar winds in the superbubble. Therefore, we also fitted the spectra using a plane-parallel shock plasma model with separate ion and electron temperatures, $kT_a$ and $kT_b$, respectively (NPSHOCK, Borkowski et al. 2001). The fit parameters are given in Table 2.

As can be seen in Table 2, $kT_a$ and $kT_b$ for region 1 are almost equal and the $\chi^2$ values for the NEI and the NPSHOCK fits are comparable. Therefore, the usage of the NPSHOCK model does not seem to be necessary for region 1. In addition, the value for $\tau$ is $> 10^{11}$ s cm$^{-3}$ for both NEI and NPSHOCK models, indicating that the gas in region 1 seems to be closer to CIE than in the superbubble in N 158. The temperature of $kT = 0.54$ keV determined for region 1 is higher and more accurate than the result of the *ROSAT* PSPC analysis for this field (0.3 keV, Sasaki et al. 2002). This shows that we were only able to see the overall characteristic of a larger region with PSPC, whereas with EPIC we can now resolve smaller (few arcminutes) structures of the hot ISM.

The hot plasma in the superbubble of the H II region N 158 does not seem to be consistent with thermal equilibrium, as indicated by the low ionisation timescale $\tau = 1.4 \times 10^{10}$ s cm$^{-3}$ of the NEI fit. The temperature of the NEI fit and the ion temperature of the NPSHOCK fit are relatively high at $kT = 0.91$ keV and $kT_a = 1.0$ keV, respectively, while the electron temperature

**Table 2.** Spectral parameters obtained from the fits of the EPIC data for region 1 and the superbubble.

| Parameter | Region 1 | Superbubble |
|---|---|---|
| | NEI | |
| $N_{\rm H\,LMC}$ [$10^{22}$ cm$^{-2}$] | 0.14 (0.08–0.23) | 0.43 (0.38–0.51) |
| $kT$ [keV] | 0.54 (0.51–0.58) | 0.91 (0.74–1.1) |
| $\tau$ [$10^{11}$ s cm$^{-3}$] | 2.0 (1.6–2.4) | 0.14 (0.12–0.18) |
| *norm* ($10^{-4}$) | 2.0 (1.6–2.4) | 9.5 (8.0–13.) |
| $\chi^2$/d.o.f. | 94.81/61 = 1.55 | 185.06/106 = 1.75 |
| | NPSHOCK | |
| $N_{\rm H\,LMC}$ [$10^{22}$ cm$^{-2}$] | 0.19 (0.12–0.32) | 0.29 (0.20–0.33) |
| $kT_a$ [keV] | 0.55 (0.00–0.59) | 1.0 (0.74–1.2) |
| $kT_b$ [keV] | 0.51 (0.00–0.59) | 0.13 (0.00–0.57) |
| $\tau$ [$10^{11}$ s cm$^{-3}$] | 8.8 (5.4–12.) | 1.3 (1.0–2.3) |
| *norm* ($10^{-4}$) | 5.0 (4.2–6.3) | 11. (9.–13.) |
| $\chi^2$/d.o.f. | 91.02/60 = 1.52 | 131.79/99 = 1.33 |

**Notes.** The numbers in brackets are 90% confidence ranges. The parameter *norm* is the normalisation of the model in XSPEC and corresponds to the emission measure. For the other parameters, see Sect. 2.2.4.

is one order of magnitude lower at $kT_b = 0.13$ keV. In addition to the Galactic foreground column density, a relatively high absorption column density of $N_{\rm H\,LMC,N158} = 4.3$ or $2.9 \times 10^{21}$ cm$^{-2}$ was determined. In comparison, the total column density in the LMC is $N_{\rm H\,LMC} = 1.0{-}5.5 \times 10^{21}$ cm$^{-2}$ (Brüns et al. 2005). This corroborates that the diffuse X-ray emission most likely arises from inside the shell of the superbubble.

## 3. Discussion

To the east of PSR B 0540−69, the diffuse emission seems to arise from ionised gas close to thermal equilibrium with a temperature comparable to the value determined from the *ROSAT* PSPC spectrum. In contrast, a shorter ionisation timescale and higher temperatures are found in the south. Since the emission coincides spatially with the superbubble in the H II region N 158, we conclude that the origin of the diffuse X-ray emission is the hot gas within the interstellar bubble. The gas in the bubble interior is shocked by stellar winds, and the cooler outer rim is visible as an H II region. The total unabsorbed X-ray luminosity of the bubble is $L_{\rm X}(0.2{-}10.0\ {\rm keV}) = 1.5 \times 10^{36}$ erg s$^{-1}$. Stars with masses over 25 $M_\odot$ are luminous X-ray emitters with luminosities of $L_{\rm X}(0.2{-}10.0\ {\rm keV}) \approx 10^{33}$ erg s$^{-1}$. In LH 104, there are 16 stars with masses above 25 $M_\odot$ (Testor & Niemela 1998, see also Sect. 3.2 for details), which account for $L_{\rm X}(0.2{-}10.0\ {\rm keV}) \approx 1{-}2 \times 10^{34}$ erg s$^{-1}$. This is two magnitudes lower than the emission from the bubble and can be neglected in the following discussion.

The comparison of the X-ray emission with the H$\alpha$ shell in Fig. 2 shows that there is additional X-ray emission outside the H$\alpha$ shell, which might indicate that some hot gas escaped the superbubble. This was also suggested by Dunne et al. (2001) based on the analysis of *ROSAT* data, which had already shown that the X-ray emission is not confined by the H$\alpha$ shell. However, we are unable to rule out that some projection effect might make the H$\alpha$ look smaller than the extent of the X-ray emission.

### 3.1. Results of the spectral analysis

For more advanced studies, we used the NEI fit results for region 1 and NPSHOCK fit results for the superbubble. The emitting volume could be approximated by an ellipsoid, although it is deformed in the south. We derived the radii from the EPIC mosaic image: $a = 4' \pm 1' = (56 \pm 14)$ pc, $b = 3' \pm 1' = (42 \pm 14)$ pc ($D_{\rm LMC} = 48$ kpc). We were unable to determine the third radius of the assumed ellipsoid. Therefore, we assumed that the superbubble is oblate and has a configuration similar to that of a disk perpendicular to the plane of the sky, i.e., also perpendicular to the disk of the LMC ($c = a$). The volume of the bubble is then $V = 4/3\,\pi\,abc = (1.62 \pm 0.03) \times 10^{61}$ cm$^3$. With the LMC metallicity $\zeta_{\rm LMC} = 0.5$, we find that $n_{\rm e} = (1.2 + 0.013\zeta_{\rm LMC})\,n \approx 1.21\,n$, where $n$ is the hydrogen density. Therefore, the normalisation of the spectral fit is

$$\begin{aligned} norm &= \frac{1}{10^{14} \times 4\pi D_{\rm LMC}^2} \int n_{\rm e} n \,{\rm d}fV \\ &\approx \frac{1}{10^{14} \times 4\pi D_{\rm LMC}^2}\, 1.21\, n^2\, f\, V \\ &= 4.4 \times 10^{-62}\, n^2\, f\, V \ \left[{\rm cm}^{-5}\right], \end{aligned} \tag{1}$$

where $f$ is the filling factor, and the gas density within the bubble can be estimated as

$$n = 4.8 \times 10^{30} \times \sqrt{\frac{norm}{f\,V}} \ \left[{\rm cm}^{-3}\right]. \tag{2}$$

Using $norm = (1.1 \pm 0.2) \times 10^{-3}$ from the fit with the NPSHOCK model, we get $n = (4.0 \pm 0.7) \times f^{-1/2} \times 10^{-2}$ cm$^{-3}$. If $f < 1$, then the density of $n = 4.0 \times 10^{-2}$ cm$^{-3}$ is a lower limit. However, the angular resolution of the X-ray data does not allow us to unambiguously determine the filling factor. For a young interstellar bubble such as in N 158, the filling factor can be assumed to be $f \approx 1$.

With temperature $T_a = (1.0 \pm 0.2)$ keV and density $n$ given, the pressure of the gas is

$$\begin{aligned} P/k &= (n_{\rm e} + 1.1n) f^{-1/2} T_a = 2.31 n f^{-1/2} T_a \\ &= (1.1 \pm 0.3) \times f^{-1/2} \times 10^6 \ {\rm cm}^{-3}\ {\rm K}. \end{aligned} \tag{3}$$

While the pressure of the Galactic ISM is thought to be $P/k = 10^{3-4}$ cm$^{-3}$ K, star-forming regions in general have higher pressures of the order of $P/k = 10^{5-6}$ cm$^{-3}$ K. For a galaxy such as the LMC with a high star-formation rate, Oey & García-Segura (2004) estimated an ISM pressure of $P/k \approx 10^5$ cm$^{-3}$ K. Thus, the pressure inside the superbubble in N 158 is about ten times higher than in the surrounding hot ISM. de Avillez & Breitschwerdt (2005) performed a 3D simulation of the ISM including the effect of magnetic fields and obtained a map of the distribution of temperature, pressure, magnetic field, etc. They showed that in regions where the temperature is about $10^{5-6}$ K, the pressure is $P/k = 10^{4-5}$ cm$^{-3}$ K, but can reach $P/k > 10^5$ cm$^{-3}$ K in the interior of hot bubbles. This is in agreement with the pressure that we obtain from the X-ray spectrum of the superbubble.

The part of the LMC in which N 158 is located in general shows faint diffuse X-ray emission indicative of hot ISM. The region that we call region 1 is particularly bright and allows us to estimate the foreground column density causing the absorption of the soft X-rays. The shell of cooler gas around the superbubble should form an additional absorbing component. Using the absorbing column density determined for region 1 (besides the

Galactic column density) as the mean LMC value $N_{\rm H\,LMC,\,region1} = (1.4 \pm 0.9) \times 10^{21}$ cm$^{-2}$, the column density of the shell around the superbubble is $N_{\rm H\,shell} = N_{\rm H\,LMC,\,N158} - N_{\rm H\,LMC,\,region1} = (1.5 \pm 1.3) \times 10^{21}$ cm$^{-2}$.

### 3.2. Analytic estimates

With the values derived from spectral fitting for pressure and density inside the bubble, we inferred a thermal energy content of $E(t) = 3/2 \times P \times f \times V = 3.6 \times f^{1/2} \times 10^{51}$ erg. We estimated a mean shell thickness of ~0.′5, i.e., ~ 10% of $a$, corresponding to ~7 pc from the MCELS H$\alpha$ image shown in Fig. 2. From the column density $N_{\rm H\,shell}$ calculated in the last section, we obtained a density of $n_{\rm shell} \approx 70\,{\rm cm}^{-3}$ inside the shell. Since the ISM around N 158 shows H$\alpha$ emission, its temperature is probably around 8000 K, typical of the warm ionised medium (McKee & Ostriker 1977), resulting in a speed of sound of ~9.2 km s$^{-1}$. With the inferred pressure of $P/k = 1.1 \times f^{-1/2} \times 10^6$ cm$^{-3}$ K from Eq. (3), we obtained a density of the ambient medium of ~13 cm$^{-3}$, yielding a compression factor of the shock of ~6. Since the cooling time behind the shock is very short because of the high density in the shell, the shock will be isothermal and, as shown below, also strong. Since we now know the radius, energy content, and density, we can use the solution for a wind blown bubble by Weaver et al. (1977) to find out the age of the bubble, which is about $t \simeq 1.1$ Myr resulting in an energy input rate over this time interval of $L_{\rm superbubble} = 2.3 \times 10^{38}$ erg s$^{-1}$. In addition, the mass inside a homogeneous bubble is $M = 2.31 n \times \mu \times m_{\rm H} \times V = 770\ M_\odot$, where $\mu = 0.61$ is the mean molecular weight of a fully ionised gas and $m_{\rm H}$ is the hydrogen mass. Thus, a mass-loss rate of $6.9 \times 10^{-4}\ M_\odot$ yr$^{-1}$ over 1.1 Myr is derived. In the following, we discuss whether massive stars can account for such a large mass-loss and energy input rate.

To calculate the mass loss and energy input rates of OB stars (in cgs units), we use the mass-luminosity relation for stars with $10 \le M/M_\odot \le 50$ by Vitrichenko et al. (2007) to obtain the mass $M$ and luminosity $L_\star$ of a star with bolometric magnitude $M_{\rm bol}$

$$M_{\rm bol} = 1.6\text{–}6.9 \log(M/M_\odot), \quad (4)$$

$$L_\star = 19 (M/M_\odot)^{2.76} L_\odot. \quad (5)$$

The radius of the star is obtained from

$$R = \sqrt{\frac{L_\star}{4\pi\sigma T_{\rm eff}^4}}, \quad (6)$$

where $T_{\rm eff}$ is the effective temperature of the star and $\sigma$ is the Stefan-Boltzmann constant. Both $M_{\rm bol}$ and $T_{\rm eff}$ are taken from Table 2 of Testor & Niemela (1998). The wind velocity is determined according to the theory of radiation-driven winds (Castor et al. 1975)

$$v_\infty = a v_{\rm esc} = a \left[ \frac{2GM}{R} \times (1 - L_\star / L_{\rm edd}) \right]^{0.5}, \quad (7)$$

where $a \simeq 2.5$ (Lamers et al. 1995). The parameter $v_{\rm esc}$ is the photospheric escape velocity and the Eddington luminosity is $L_{\rm edd} = 4\pi G \times M \times m_{\rm p} \times c/\sigma_{\rm T}$, where $m_{\rm p}$ is the mass of a proton and $\sigma_{\rm T}$ the Thomson cross-section for the electron. The mass loss is determined from the single-scattering limit

$$\dot{M} = \frac{L_\star}{v_\infty \times c}. \quad (8)$$

We corrected for the LMC metallicity $\zeta_{\rm LMC}$ following Leitherer et al. (1992) and obtained $\dot{M} \propto \zeta_{\rm LMC}^{0.8}$ for the mass loss and $v_\infty \propto \zeta_{\rm LMC}^{0.13}$ for the wind velocity (for hot stars with $M > 15 M_\odot$). Thus, the 67 O- and B-stars in LH 104 produce a mass loss of ~39 $M_\odot$ or an energy input rate of $L_{\rm OB} = 3.4 \times 10^{37}$ erg s$^{-1}$ over 1.1 Myr.

Additionally, the Wolf-Rayet (WR) stars generate ~35 $M_\odot$ or $L_{\rm WR} = 1.8 \times 10^{38}$ erg s$^{-1}$, but only for $2.5 \times 10^5$ yr $\cong 0.23\ t$, assuming that they already went through half of their WR-lifetime of $\sim 5 \times 10^5$ yr (Maeder & Meynet 1987). The mass loss and wind velocity of WR-binaries are adopted from Leitherer et al. (1997) and corrected for mass losses of WC and WN types in the LMC according to Crowther (2007). Furthermore, we have to calculate the contribution of winds from WR-binaries before entering the WR-phase, i.e., for the remaining 0.85 Myr. With mass losses for O6 and O7-stars and O4-stars as WR-progenitors (PR) taken from Garmany et al. (1981) and velocities from Lamers & Leitherer (1993), we get 4 $M_\odot$ or $L_{\rm PR} = 8.0 \times 10^{36}$ erg s$^{-1}$ for 0.85 Myr $\cong 0.77\ t$ from these stars.

In total, we find that winds can account for ~78 $M_\odot$ or a mechanical luminosity of $L = 8.0 \times 10^{37}$ erg s$^{-1}$ over 1.1 Myr. Nevertheless, most of the mass (~690 $M_\odot$) or $L_{\rm superbubble} - L = 1.5 \times 10^{38}$ erg s$^{-1}$ corresponding to a thermal energy of $2.3 \times 10^{51}$ erg is "missing", but this can be partly explained after applying an IMF to the star cluster. According to the Hertzsprung Russell diagram (HRD) of Testor & Niemela (1998, Fig. 6b) and using the masses derived from the $M$-$L$ relation (Vitrichenko et al. 2007), we find that 16 stars in LH 104 have masses above 25 $M_\odot$ including all O-stars, WR-binaries, the B0V stars with Id 4–41 and 4–55, and Sk-69 259. As an upper mass limit, we take 65 $M_\odot$ as a rough estimate, since Massey et al. (2000) suggested that the progenitor masses of WR-stars in this cluster should be in excess of 60 $M_\odot$. On the other hand, by looking at the HRD of LH 104 in Massey et al. (2000, Fig. 7) we find at least 20 stars in the 25–65 $M_\odot$ interval for which spectral types or photometry are available. Comparing both HR-diagrams shows that the total number of member stars is quite uncertain, but there must be at least 70 stars with masses above 8 $M_\odot$.

Assuming that all stars formed from the same parental cloud and using an IMF with $\Gamma = -1.05$ (Testor & Niemela 1998), we obtain a total of 74 stars between 8 and 65 $M_\odot$ in the first case (16 stars with $25 < M/M_\odot < 65$) and 93 stars in the other case (20 stars with $25 < M/M_\odot < 65$). In both cases, there are about two stars in the 65–80 $M_\odot$ mass interval or about three stars in the 65–90 $M_\odot$ mass interval. This suggests that 2–3 supernovae (SNe) already exploded around 1 Myr ago and that with $E_{\rm SN} = 10^{51}$ erg per SN explosion, they can easily account for the required amount of energy. These 2–3 SNe yield approximately 150–240 $M_\odot$ of ejecta mass, thus the production of 230–310 of the 770 solar masses in the bubble can be explained. Any remaining discrepancies should be due to mass loading and the evaporation of entrained interstellar clouds and/or turbulent mixing of material from the cold shell.

With the parameters determined so far, we can further investigate the geometry of the bubble and the ambient ISM. We use an analytical model for the expansion of a wind-blown bubble in an exponentially stratified medium symmetric to the galactic midplane (Baumgartner & Breitschwerdt, in prep.) based on the approximation of Kompaneets (1960). With an energy input rate of $L_{\rm superbubble} = 2.3 \times 10^{38}$ erg s$^{-1}$, the bubble should reach a radius, i.e., semi-major axis, of 56 pc after ~1.1 Myr. We calculated models with different scale heights ($H = 50$, 100, and 500 pc) and obtain a density of the ambient medium of $n_0 = 9$, 11, and 13 cm$^{-3}$, respectively. Values for the height of

the bubble above/below the galactic plane are $c = 80, 66$, and 58 pc. Using $b = 42$ pc, we obtain a volume of the bubble of $V = 2.4 \times 10^{51}$ cm$^3$, $1.9 \times 10^{61}$ cm$^3$, and $1.7 \times 10^{61}$ cm$^3$. Since a larger elongation, i.e., lower scale height, yields a larger volume, we argue that a larger scale height provides a close fit, otherwise the density inside the bubble is too low. With $V = 1.7 \times 10^{61}$ cm$^3$ and *norm* from Sect. 3.1, we derive $n = 3.9 \times 10^{-2}$ cm$^{-3}$. This is close to the value that was used to calculate the mass inside the bubble and the energy input rate in the beginning, whereas a volume of $V = 2.4 \times 10^{51}$ cm$^3$ for $H = 50$ pc yields only $n = 3.2 \times 10^{-2}$ cm$^{-3}$. The shell thickness in the case of $H = 500$ pc is ~5 pc resulting in a density of the shell of 100 cm$^{-3}$, which is somewhat higher than the density of 70 cm$^{-3}$ derived from the observation. Finally, we calculated the velocity of 31 km s$^{-1}$ for the outer shock, which propagates into the ambient warm medium at the top/bottom of the bubble, and found that it agrees very well with the expansion velocity found for the wind solution of Weaver et al. (1977). This velocity corresponds to a Mach number of $M \sim 3.4$. For comparison, Dunne et al. (2001) reported an expansion velocity of the superbubble of $v_{\rm exp} \approx 45$ km s$^{-1}$ assuming a pressure-driven bubble in an homogeneous medium. The magnetic fields in the ISM of the LMC are on the order of ~1 $\mu$G (Gaensler et al. 2005) corresponding to an Alfvén velocity of ~0.5 km s$^{-1}$. Therefore, the effects of the magnetic fields are negligible.

## 4. Summary

We have found significant diffuse X-ray emission in the field of view of the *XMM-Newton* observations of the pulsar B 0540−69, which is not related to the pulsar. The analysis of the spectrum of the emission has shown that it is purely thermal and can be best modelled with a hot shocked gas. The extended diffuse emission coincides spatially with the superbubble in the H II region N 158 in the LMC. Therefore, we conclude that the origin of the X-ray emission is the hot gas inside the superbubble in N 158.

From the parameters obtained from the analysis of the *XMM-Newton* spectra, we have derived a temperature of $kT = 1$ keV, a density of $n = 0.04$ cm$^{-3}$, and a pressure of $P/k = 10^6$ cm$^{-3}$ K inside the superbubble. These results enable us to perform analytic calculations of the evolution of the superbubble. Since the OB association LH 104 that is located inside the superbubble has been studied in detail (Testor & Niemela 1998), the stellar population inside the superbubble is well known. Using its IMF and HRD, we have calculated the mass loss and energy input rates of the stars. We have estimated an age of ~1 Myr and a total energy input rate of $L = 2.3 \times 10^{38}$ erg s$^{-1}$. The massive stars including WR-stars and binaries in LH 104 account for $L = 8 \times 10^{37}$ erg s$^{-1}$. Therefore, to reproduce the observations, there should have been 2−3 SN explosions in the past 1 Myr. We have also performed calculations of the expansion of the superbubble for different scale heights. We have demonstrated that a large scale height of $H = 500$ pc can closely reproduce the observed density inside the superbubble as well as the density in the shell around it. The corresponding expansion velocity of the superbubble is also in good agreement with the model of Weaver et al. (1977).

*Acknowledgements.* The authors thank the anonymous referee for comments that helped to improve the paper. This research is based on observations obtained with *XMM-Newton*, an ESA science mission with instruments and contributions directly funded by ESA Member States and NASA. We have also made use of preliminary data of the UM/CTIO Magellanic Cloud Emission Line Survey (MCELS) available on the web site of the project (http://www.ctio.noao.edu/mcels/). M.S. acknowledges support by the Deutsche Forschungsgemeinschaft through the Emmy Noether Research Grant SA 2131/1. V.B. is recipient of a DOC-fFORTE fellowship of the Austrian Academy of Sciences.

## References

Aschenbach, B., Briel, U. G., Haberl, F., et al. 2000, Proc. SPIE, 4012, 731
Borkowski, K. J. 2000, in Rev. Mex. Astron. Astrofis. Conf. Ser., 9, 288
Borkowski, K. J., Lyerly, W. J., & Reynolds, S. P. 2001, ApJ, 548, 820
Brüns, C., Kerp, J., Staveley-Smith, L., et al. 2005, A&A, 432, 45
Carter, J. A., & Read, A. M. 2007, A&A, 464, 1155
Castor, J., Weaver, R., & McCray, R. 1975, ApJ, 200, L107
Chu, Y., Chang, H., Su, Y., & Mac Low, M. 1995, ApJ, 450, 157
Crowther, P. A. 2007, ARA&A, 45, 177
de Avillez, M. A., & Breitschwerdt, D. 2005, A&A, 436, 585
Dickey, J. M., & Lockman, F. J. 1990, ARA&A, 28, 215
Dunne, B. C., Points, S. D., & Chu, Y. 2001, ApJS, 136, 119
Gaensler, B. M., Haverkorn, M., Staveley-Smith, L., et al. 2005, Science, 307, 1610
Garmany, C. D., Olson, G. L., van Steenberg, M. E., & Conti, P. S. 1981, ApJ, 250, 660
Henize, K. G. 1956, ApJS, 2, 315
Jansen, F., Lumb, D., Altieri, B., et al. 2001, A&A, 365, L1
Kompaneets, A. S. 1960, Sov. Phys. Dokl., 5, 46
Lamers, H. J. G. L. M., & Leitherer, C. 1993, ApJ, 412, 771
Lamers, H. J. G. L. M., Snow, T. P., & Lindholm, D. M. 1995, ApJ, 455, 269
Leitherer, C., Robert, C., & Drissen, L. 1992, ApJ, 401, 596
Leitherer, C., Chapman, J. M., & Koribalski, B. 1997, ApJ, 481, 898
Lucke, P. B., & Hodge, P. W. 1970, AJ, 75, 171
Macri, L. M., Stanek, K. Z., Bersier, D., Greenhill, L. J., & Reid, M. J. 2006, ApJ, 652, 1133
Maeder, A., & Meynet, G. 1987, A&A, 182, 243
Massey, P., Waterhouse, E., & DeGioia-Eastwood, K. 2000, AJ, 119, 2214
McKee, C. F., & Ostriker, J. P. 1977, ApJ, 218, 148
Oey, M. S., & García-Segura, G. 2004, ApJ, 613, 302
Petre, R., Hwang, U., Holt, S. S., Safi-Harb, S., & Williams, R. M. 2007, ApJ, 662, 988
Read, A. M., & Ponman, T. J. 2003, A&A, 409, 395
Russell, S. C., & Dopita, M. A. 1992, ApJ, 384, 508
Sasaki, M., Haberl, F., & Pietsch, W. 2002, A&A, 392, 103
Sasaki, M., Plucinsky, P. P., Gaetz, T. J., et al. 2004, ApJ, 617, 322
Schild, H., & Testor, G. 1992, A&AS, 92, 729
Strüder, L., Briel, U., Dennerl, K., et al. 2001, A&A, 365, L18
Testor, G., & Niemela, V. 1998, A&AS, 130, 527
Turner, M. J. L., Abbey, A., Arnaud, M., et al. 2001, A&A, 365, L27
Vitrichenko, E. A., Nadyozhin, D. K., & Razinkova, T. L. 2007, Astron. Lett., 33, 251
Weaver, R., McCray, R., Castor, J., Shapiro, P., & Moore, R. 1977, ApJ, 218, 377